Optical, electrical, and acetone sensing properties of 3D networks of Ge quantum wires and nanopores in Al_2O_3 matrix doped with Nb and Ta

Optical, electrical and sensor properties of 3D networks of Ge quantum wires and nanopores embedded in an Al_2O_3 matrix doped with Ta and Nb

Marija Tkalčević[1], Ivana Periša[1], Krešimir Salamon[1], Matej Bubaš[1], Sigrid Bernstorff[2], Maja Mičetić[1]*

[1] Ruđer Bošković Institute, Bijenička cesta 54, 10000 Zagreb, Croatia
[2] Elettra Sincrotrone, S.C.p.A., Strada Statale 14, km 163.5 in AREA Science Park, 34149 Basovizza/Trieste, Italy

*Correspondence: Maja.Micetic@irb.hr

Abstract:

Three-dimensional (3D) networks of semiconductor quantum wires (QWs) and nanopores (NPs) show exciting properties and are usually very suitable for various applications such as sensors, catalysts, photovoltaic cells etc. Here we investigate structural, optical, electrical and acetone-sensing properties of 3D networks of Ge QWs and NPs embedded in an amorphous alumina matrix doped with Nb and Ta. The materials based on Ge QWs are produced by self-assembling growth using magnetron sputtering deposition, and the materials with NPs by their annealing. The annealing causes the evaporation of Ge from the alumina matrix, leaving a 3D mesh of nanopores with the same geometrical properties as the Ge QWs present before the annealing. We compare the properties of these two types of materials and explore the effects of Nb and Ta doping. We show that doping drastically changes the optical, electrical, and photocurrent generation properties of the materials based on Ge QWs. Their conductivity significantly increases with doping. However, the doping diminishes the photo-generation properties because it causes a substantial increase in the dark current. The materials based on NPs have entirely different optical properties, with a very low extinction coefficient for a large range of energies and a significantly lower refraction index. The conductivity of the annealed materials is several orders of magnitude smaller than in the QW-based materials. However, the NP-based materials, i.e. the Nb- and Ta- doped nanoporous alumina, show a high sensitivity of resistance to exposure to acetone vapor. Therefore, they can be potentially used as active materials in acetone sensors.

Keywords: Ge quantum wires; nanopore mesh; thin films; acetone sensor; Nb- and Ta- doped alumina;

1. Introduction

Materials based on quantum structures and nanoporous materials attract scientific interest due to their remarkable properties and potential applications in many areas, such as drug delivery systems, sensors, catalysis, photovoltaic cells, and fuel cells [1–4]. Semiconductor quantum structures like quantum dots (QDs) and quantum wires (QWs) are extensively explored because they show many exciting features like size-tuneable band gap, multiple exciton generation, size-tuneable optical and mechanical properties etc. [5–7]. Due to these features, such materials are widely applied in nanotechnology, medicine, industry, and many other fields [8,9]. Their properties and applications depend strongly on the size and shape of the embedded nanostructures or nanopores [10–18].

The application of nanostructures in acetone detection has attracted much attention because acetone is flammable and explosive, and long-term exposure to acetone vapours can cause headaches, nausea, muscle weakness, loss of coordinated speech, narcosis, or even damage to the nervous system [19,20]. In addition, acetone detected in human breath can be used for diabetes monitoring since the body produces excess amounts of ketones such as acetoacetate, beta-hydroxybutyrate, and acetone [19,21].

Germanium quantum structures show a strong confinement effect, so their properties can be tuned in a large range of values by small size or shape changes [22–26]. Another attractive property of Ge-based quantum structures is their affinity to self-assemble in regular 3D meshes during their growth by magnetron sputtering deposition. Ge QWs in the alumina matrix are interesting since they form a regular, interconnected 3D mesh with strongly tuneable network parameters [23,24,27,28]. These materials show tuneable optical properties and multiple exciton generation, which are very important for their application in super-efficient photo-sensitive devices. In our previous work, we have shown that doping with nitrogen during their production enormously improves photo-current generation properties and causes multiple exciton generation, leading to quantum efficiency larger than 150% for some energies of the incident light [24]. Therefore, the investigation of the effects of doping is of high interest.

These materials show another very interesting property when they are annealed under specific conditions [22,27]. Annealing in a low vacuum promotes Ge desorption from the matrix leaving behind a 3D mesh of nanopores in the alumina matrix with the same geometrical properties as Ge QWs present before annealing. Due to the large range of the geometrical properties of the Ge QWs mesh, it is possible to produce nanoporous films with different porosities and geometrical parameters from them. Porous thin films have a high surface-to-volume ratio, which is essential for sensing applications since it increases their ability to interact with the medium using small amounts of material. A porous configuration in sensing layers is considered the most fundamental strategy to provide larger active surface areas [10,12,29]. Alumina has excellent thermal, dielectric, and mechanical properties, including semitransparency, insolubility, and biocompatibility, making the material a good choice for gas sensing [30]. Recent investigations have shown that the metal oxides based on Nb and Ta strongly improve the sensing properties of nanoporous materials, especially in acetone sensing applications [31]. Tantalum is chemically stable and biocompatible, so it is becoming a promising material for use in biomedical implants [15,16]. Tantalum (V) oxide (Ta_2O_5) is an excellent photocatalytic material that is used for removing organic compounds from water [17,32]. Niobium (V) oxide (Nb_2O_5) thin films are often used as high-index and low-loss materials; for example, they can be used as optical waveguides' interference filters, anti-reflective coatings, or electroluminescent devices [18,31].

So, the materials based on Ge QWs in the alumina matrix offer plenty of exciting properties and possibilities for usage in photo-sensitive devices and sensors. The doping of the alumina matrix seems to be the critical parameter for optimising the mentioned materials for particular applications.

Therefore, in this work, we investigate materials based on Ge QWs and NPs in an alumina matrix doped with Nb and Ta. The effects of doping the alumina matrix with Nb and Ta on materials' structural,

electrical, and optical properties are explored. We show that doping strongly affects the optical and electrical properties of the materials based on Ge QWs, while the structural properties, including regular 3D mesh formation, do not change significantly. Although doping increases the materials' conductivity, its photo-current generation diminishes due to a strong dark current generation. The nanoporous materials obtained by evaporation of Ge QWs during annealing have entirely different optical and electrical properties. The refraction index and extinction coefficient are significantly lower for a wide range of energies than in the Ge-based materials, and their conductivity drops several orders of magnitude. The structural analysis indicates the formation of Nb_2O_5 and Ta_2O_5 nanoparticles during the annealing process. Probably due to that fact, the doped nanoporous materials show up-and-coming acetone sensing properties. The Nb-doped film shows an immediate, significant change in conductivity when exposed to acetone vapour. The Ta-doped thin films also show a drop in conductivity but with a smaller amount, while the non-doped films show a slower and smaller change.

2. Materials and Methods

2.1 Sample preparation

Magnetron sputtering has become widely popular for thin film deposition because of its high process control and homogeneity on a large deposition area. All thin films were prepared using a CMS-18 system from Kurt J. Lesker Company. The base pressure in the chamber was $8 \cdot 10^{-6}$ Pa, and the working gas (Ar) pressure was 0.46 Pa in a continuous flow. The samples were deposited on Si (100) and quartz substrates. We have used 3-inch Ge (99.999%), Al_2O_3 (99.999 %), Nb (99.999 %), and Ta (99.999 %) targets produced by K. J Lesker.

Before deposition, the substrates were cleaned in an ultrasonic bath with acetone, ethanol, and isopropanol for 5 minutes to remove any dirt and grease. Before loading in the deposition chamber, the substrates were cleaned with deionized water and dried in nitrogen gas.

The samples were named by the deposition power of the transition metal, while the alumina and the germanium power were constant for all depositions. The sample names and sputtering conditions can be found in Table 1. The sample denoted by *A* is prepared the same way as others, except for the absent Nb and Ta doping, so it is used as a control sample.

Table 1. Deposition and annealing parameters of the produced films. *P* denotes the sputtering powers of the corresponding targets, T_d is the deposition temperature t_d is the deposition time, and T_a is the annealing temperature.

Name	P_{Ge} (W)	P_{Al2O3} (W)	P_{Ta} (W)	P_{Nb} (W)	T_d (°C)	t_d (min)	T_a (°C)
A	10	130	0	0	500	60	590
Ta1	10	130	1	0	500	60	590
Ta3	10	130	2	0	500	60	590
Ta5	10	130	3	0	500	60	590
Nb1	10	130	0	1	500	60	590
Nb3	10	130	0	2	500	60	590
Nb5	10	130	0	3	500	60	590

2.2. Annealing

The annealing conditions were chosen to ensure conditions for Ge desorption. The samples were capsulated in a quartz tube and heated in an electric furnace for lab heat treatment. The annealing was performed in a low vacuum (3 mbar) at 590 ℃ for 5 minutes, followed by cooling in the low vacuum for 30 minutes. Annealing in a low vacuum ensures Ge desorption from thin films leaving a porous alumina structure behind. After the annealing, the brown-coloured samples on the quartz substrate become optically transparent due to Ge evaporation [22,27].

2.3 Structural characterization

We used grazing incidence small-angle X-ray scattering (GISAXS) and grazing incidence wide-angle X-ray scattering for structural characterization (GIWAXS). The GISAXS and GIWAXS measurements were performed at the Australian SAXS beamline of the synchrotron Elettra (Trieste, Italy). A photon energy of 8 keV, a 2D Pilatus3 1M detector (GISAXS), and a 2D Pilatus 100k detector (GIWAXS) were used simultaneously. The grazing incidence angle was slightly above the critical angle. The measured GISAXS maps were analyzed using the paracrystal model described in detail in Ref. [33].

The elemental composition of samples, listed in Table 2, was measured by Time-of-flight Elastic Recoil Detection Analysis (TOF – ERDA). The measurements were done using a 20 MeV127 I6+ beam; the angle between the sample surface and the beam was 20°, and the spectrometer was placed at 37.5°.

The optical properties of the samples prepared on Si substrates were measured by spectroscopic ellipsometry using a J. A. Woollam V-Vase ellipsometer. The measurements were carried out at 65°, 70°, and 75° angles of incidence and in the spectral range between 0.57 and 5 eV. The real and imaginary parts of the refractive index were obtained by fitting simultaneously with the film thickness. The thin films were modelled using a multiple Gaussian oscillator model that has proved successful in previous work on comparable systems [25,34]. Depolarization was also considered for some samples that exhibited non-uniform thickness to ensure the fit quality between the experimental and model-based data.

The electrical properties of samples deposited on Si (100) were investigated using a PTS-2-QE System from Sciencetech. For this measurement, we deposited one contact over the film and one on the bottom of the substrate. The first was a transparent ITO (indium-doped tin oxide) contact, and the second was an aluminium contact. Both contacts were deposited using a magnetron sputtering deposition at room temperature.

Sensing tests were performed on annealed samples deposited on quartz in a lab-scale apparatus using Keithley's model 6517B. The resistance was examined at a constant operating voltage of 200 V applied across the electrodes. The measuring stage was fabricated using a 3D printer, and four gold pins were used as electrodes. The measuring setup for resistance measurements and acetone detection is shown in **Fig. 1**.

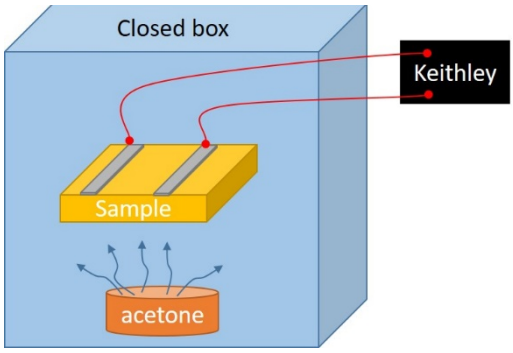

Fig. 1. The measuring setup for resistance measurements and acetone detection.

3. Results

3.1. Structural properties

3.1.1. Elemental composition

The doping of thin films containing Ge QWs with noble metals (Nb/Ta) was confirmed using Time-of-flight Elastic Recoil Detection Analysis (TOF-ERDA) measurements. TOF-ERDA is a spectroscopic technique that can measure elemental concentrations and their depth profiles. The incorporation of transition metals in thin films is confirmed, and the results are shown in **Table 2**. Concentrations were measured before and after annealing.

After the annealing, the Ge concentration is drastically reduced in all samples; however, some Ge is still present in the samples doped with noble metals. Doping of Ge QWs appears to prevent Ge from evaporation from the samples since Ge evaporates almost completely from sample *A* containing only Ge QWs in the alumina matrix, which is consistent with our previous research [22].

Table 2. The atomic percentage of Ge, Ta, and Nb in the films before and after annealing.

Name	Ge (At.%)	Ta (At.%)	Nb (At.%)	Name	Ge (At.%)	Ta (At.%)	Nb (At.%)
A	37±2	0	0	**A ann**	4±2	0	0
Ta1	32±2	2.1±0.4	0	**Ta1 ann**	11±1	1	0
Ta3	32±2	3.3±0.6	0	**Ta3 ann**	5±1	2.5±0.5	0
Ta5	31±2	6±1	0	**Ta5 ann**	5±1	5±1	0
Nb1	41±2	0	1.1±0.2	**Nb1 ann**	8±1	0	0.9±0.2
Nb3	41±2	0	1.5±0.2	**Nb3 ann**	8±1	0	1.4±0.2
Nb5	40±2	0	2.9±0.3	**Nb5 ann**	7±1	0	3.0±0.4

Germanium desorption is driven by the thermal instability of GeO_2 and the reaction that occurs at the interface of Ge/GeO_2. The mechanism of this reaction is as follows: $GeO_2 + Ge \rightarrow 2\ GeO\uparrow$ [35–37]. For specific annealing conditions, germanium evaporates from the samples with Ge quantum wires, leaving a 3D-ordered network of nanovoids in an alumina matrix. This phenomenon has been investigated previously by our group [5,22,27]. Germanium desorption was confirmed using RBS measurements and TOF-ERDA measurements. The formation of a 3D-ordered network of nanopores was confirmed using TEM and GISAXS measurements, as seen in **Fig. 2.**

A 3D model of Ge QWs in the alumina matrix is given in a). The structural parameters of the network are denoted with an *a* (in-plane separation of the nods), *c* (vertical separation of the nods), and *L* (length of the nanopore). GISAXS maps of the thin films before and after annealing are shown in b). HRTEM of the thin films before (d) and after annealing (e). The Ge quantum wires (i.e., the formed voids after annealing) are shown in red colour (c), while the empty space, in that case, represents the alumina matrix in which the nanostructures are embedded. The openings in this structure indicated by blue and yellow arrows are the places where alumina is connected to the alumina from the neighbouring unit cells. The openings to the unit cell in the same plane (plane parallel to the substrate) are indicated by blue arrows, while the openings to the planes up and below (planes perpendicular to the substrate) are indicated by yellow arrows.

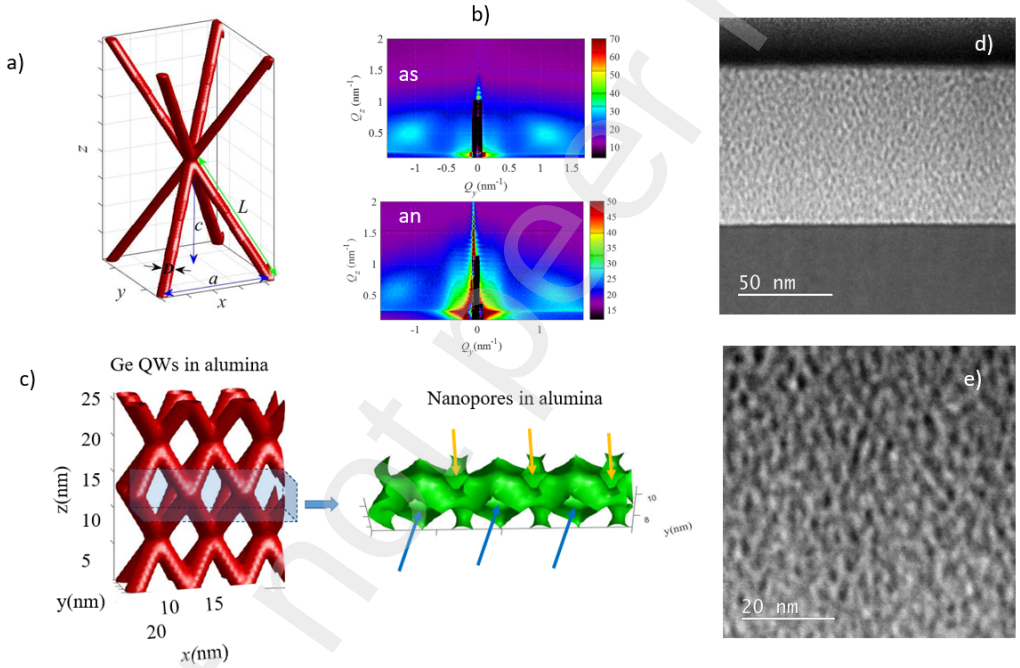

Fig. 2. 3D model of Ge NWs in alumina matrix a); GISAXS maps of thin films before and after annealing (b) in low vacuum. The porous structure of alumina is shown in c). The openings in this structure indicated by blue and yellow arrows are the places where alumina is connected to the alumina from the neighbouring unit cells HRTEM of the thin film before (d) and after annealing (e) [32].

3.1.2. Geometrical and ordering properties of QWs and nanopores

A detailed characterization of the material's size, shape, and arrangement of nanostructures is essential for precisely manipulating its properties. GISAXS is the leading technique for thin film characterization because it provides data in reciprocal space with excellent statistics over the whole sample. The regular ordering of nanostructures in a matrix causes characteristic peaks in their GISAXS maps. Their positions and widths are determined by the ordering type of the nanostructures and the degree of regularity in their ordering. This property enables already a rough estimation of the material's structure from a visual inspection of the GISAXS map.

The GISAXS maps of all the investigated films are shown in **Fig. 3.** The side peaks are visible in the GISAXS maps of all films before and after annealing, except for as-grown thin film Ta5T5. The presence of such peaks shows that the geometrical properties do not change significantly after annealing, as explained in the previous paragraph. However, the peaks in the maps of the annealed films are less pronounced and broader, indicating that the ordering quality is slightly lower. This is the consequence of a slight change in the geometry of the nanopores, which remained after the Ge evaporation. Fig. 3 (a) shows the maps of the pure alumina films (denoted by A) without doping, while the Nb- and Ta-doped films are shown in Figs. 3 (b) and (c), respectively. The GISAXS map of the Ta-doped film with the lowest doping (Ta1) is almost the same as the non-doped film. The increased Ta concentration causes lower visibility of the lateral peaks in their GISAXS maps. However, the lateral peaks in the annealed films of the same type show well-resolved lateral peaks.

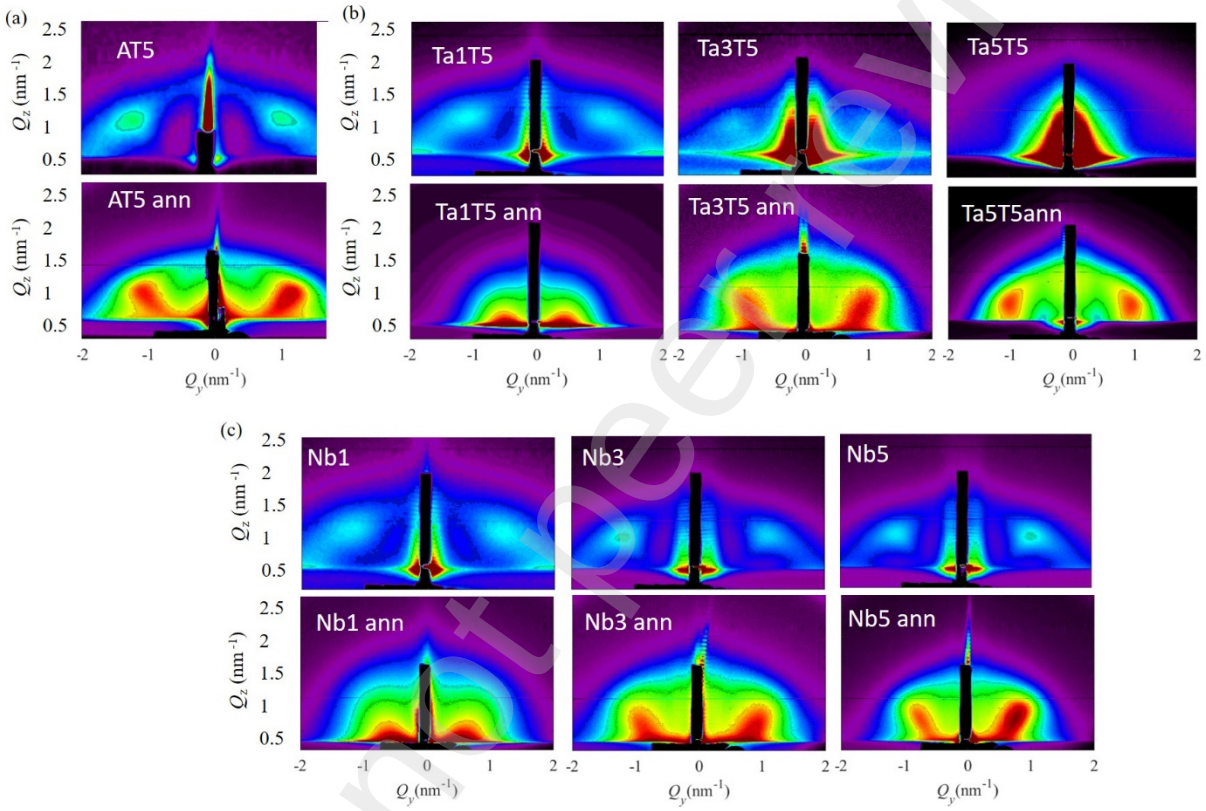

Fig. 3. GISAXS maps of (a) pure alumina films, (b) Ta-rich films, and (c) Nb-rich films before (top) and after (below) annealing.

The low visibility of the side peaks in the non-annealed Ta-containing films is due to the presence of Ta atoms, which are very heavy and thus strongly contribute to the GISAXS maps. That strong contribution of the Ta-signal covers the lateral peaks caused by the regular ordering of Ge QWs. The characteristic central semi-circular shape of the signal indicates the formation of small spherical Ta nanoparticles. So their contribution to the GISAXS map overlays the signal from the Ge QWs. The GISAXS map of the annealed Ta film (Ta5 ann) is another proof of this assumption. This map shows very clear side maxima caused by the 3D mesh of nanopores. The Ta content in the annealed films is lower, and the nanopores are present instead of Ge QWs. The nanopores make a much stronger contribution to the GISAXS map than Ge QWs because the intensity of the signal is related to the electronic density contrast between the nanostructures and the matrix. Therefore, the regularity in the ordering of nanopores is better visible in the GISAXS maps of the annealed Ta–doped films (Fig. 3(b)).

Nb-doped films show similar properties, except the lateral peaks are well visible for all Nb concentrations. Nb is lighter than Ta and has a slightly smaller atomic percentage, so it does not cover the contribution from regularity in the QW ordering.

A numerical analysis of the GISAXS maps is performed to obtain detailed information about the system's structure. For the analysis, we have assumed a short-range order type of the QWs and nanopores and a body central-tetragonal (BCT) ordering of the mesh nodes. This is in accordance with our previous investigation of the same material type without doping [22,27]. More details about the numerical analysis can be found in [38,39].

The main parameters of the formed QW and nanopore lattices (see Fig. 2 for the definitions of the parameters) are the following: lateral separation a = 6.5±0.6 nm, vertical parameter c = 4.4 ±0.4 nm, the QW/nanopore diameter D = 1.8±0.3 nm, and their length L = 6.5±0.6 nm. The parameters of the annealed films are very similar; however, the disorder of the network nodes is more significant, as can be seen in Figure. 3.

3.1.3. Crystalline properties of QWs and nanopores

The crystalline structure of the films was determined by grazing incidence wide-angle x-ray scattering (GIWAXS). The measured data for all films are presented in **Figure 4.** All films are fully amorphous before and after annealing. The as-grown films, shown in Figure 4(a), show two strong peaks related to the amorphous Ge (a-Ge) [40]. These two broad peaks are around 27 deg and 50 deg, corresponding to the Ge (111) and Ge (200) + Ge (311) peaks, respectively. In addition, weak peaks related to very small nanoparticles of Ta and Nb are visible near 38 deg and 55 deg, corresponding to the (111) and (220) peaks of cubic *Im3m* Nb and Ta. Both Ta and Nb crystallize in the same lattice, having very similar lattice parameters (3.3058 and 3.3004 Å, respectively). These peaks are the best visible for the film with the highest Ta doping (Ta5). These results additionally confirmed the results of the GISAXS measurements, in which the signal of the Ta nanoparticles covered the signal of the Ge QWs due to the stronger electronic contrast to the alumina matrix.

The GIWAXS spectra of the same films after annealing are shown in Figure 4(b). The Ge- related peaks are not visible, confirming Ge desorption from the films during annealing. The spectra show only broad peaks related to amorphous Al_2O_3 and amorphous Ta_2O_5 and Nb_2O_5 [41–43]. This result is expected since Ge evaporated from the film during annealing in a low vacuum which is oxygen-rich. The presence of oxygen causes evaporation of Ge [27], but also oxidation of Ta and Nb. So, after the annealing, the materials consist of a 3D mesh of nanopores in amorphous alumina with Nb_2O_5 and Ta_2O_5 nanoparticles.

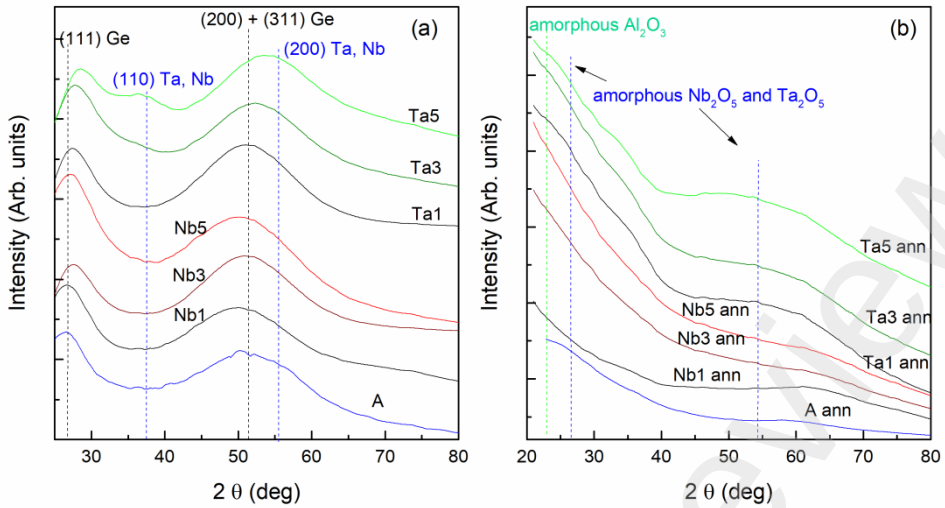

Figure 4. GIWAXS pattern of the (a) as-grown and (b) annealed thin films. Dashed vertical lines denote the peaks related to amorphous Ge, Al_2O_3, Ta_2O_5 and Nb_2O_5.

3.2. Optical properties

Here, we examine the optical properties of the films with the middle doping (Ta3 and Nb3) together with the control sample without doping (A), measured with Spectroscopic ellipsometry. The measurements of other doping concentrations show qualitatively the same results, so they are not shown here. The dependence of the materials extinction coefficient (k) and index of refraction (n) on the photon energy is shown for the films before and after annealing in **Fig. 5.** The strong influence of Nb- and Ta- doping on the optical constants n and k of the Ge QWs-containing films is visible in Figs. 5(a) and (b), respectively. The refraction index increases at lower energies by doping and decreases at energies larger than 2 eV. The extinction coefficients show the opposite trend. It is very large at low energies for the non-doped film (A) and small for the doped ones. The value of k becomes larger for the doped films for energies above 2.5 eV.

The optical properties of the films change drastically after annealing, as visible in Figs. 5(c) and (d). Both the refraction index and extinction coefficient are much lower than for the non-annealed films. However, the shape of the n and k curves are very similar for the non-doped and doped films, which was not the case for the non-annealed ones. Both values increase with doping, with a more significant increase for the Ta-doped film, as expected due to the large mass number of Ta. This strong change can be explained by the evaporation of germanium from the films and by the formation of Ta- and Nb- oxides during annealing. The measured optical properties show strong tunability of optical constant by Ta and Nb doping and the annealing treatment.

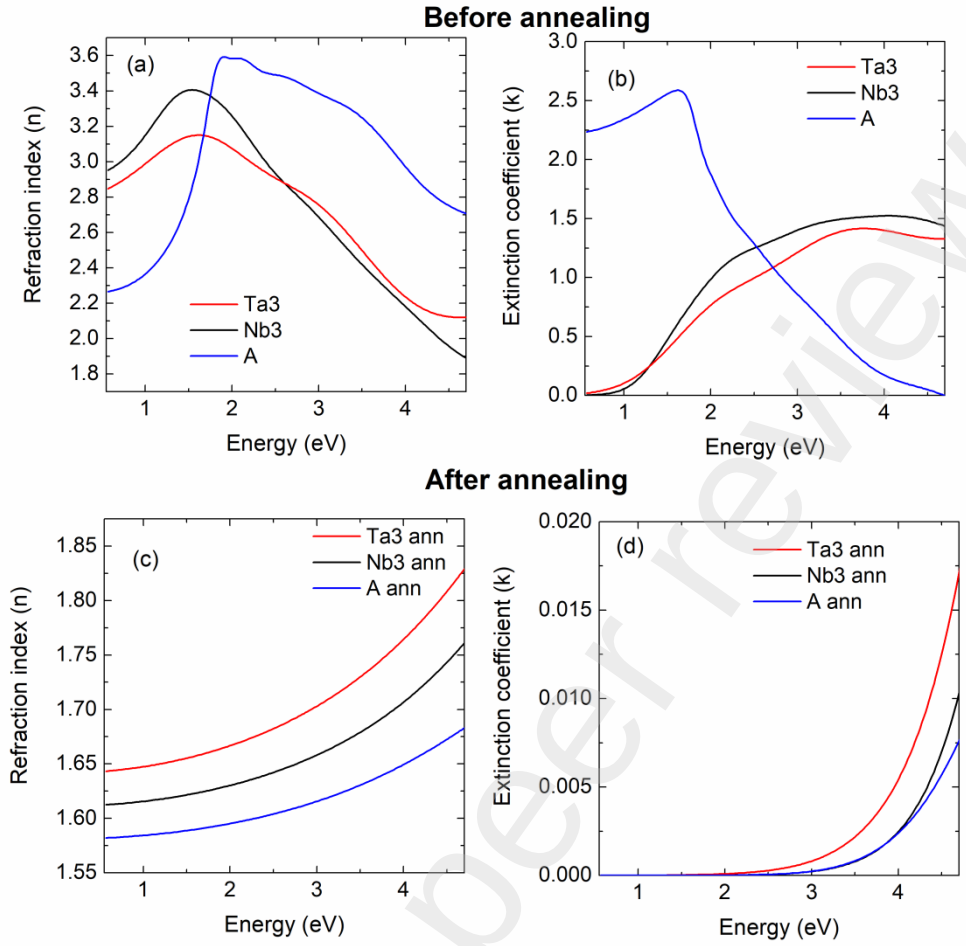

Fig. 5. Optical constants: refraction index *n* and extinction coefficient *k* of the films Ta3, Nb3, and A before and after annealing.

3.3. Electrical characterization

The results of the electrical measurements of the films with the middle doping concentration are shown in **Fig. 6**. The resistivity measurements for the films with Ge QWs (Fig. 6(a)) display a significant decrease of the resistivity with Nb- and Ta- doping (over 3 orders of magnitude). The Ta-doping results in lower film resistivity compared to Nb-doping.

Another exciting feature of Ge-QWs-based thin films is their strong photo-electric activity. Our previous investigations showed that a strong photo-current could be produced using Ge QWs-based films [24,44]. Therefore, we investigate the influence of Ta- and Nb- doping on the photoelectric generation properties. Fig. 6 (b) shows the *I-V* measurements of the non-doped and doped thin films on a Si substrate illuminated and in the dark. The measurements show that the largest difference between light and dark currents has the non-doped material (A). The doping causes an increase of both light and dark currents, so these two currents are practically the same for the doped films. The difference is slightly more significant for the Nb-doped film. Therefore, the doping is not favourable if photo-electric generation is desirable in a Ge-QW-based material.

The resistance of the films increased significantly after the annealing caused by the Ge evaporation, as visible in Fig. 6(c). The value of the increase is several orders of magnitude. Several factors cause this strong increase. The first is the evaporation of Ge, and the second is Nb and Ta's oxidation. Therefore, the materials consist of alumina with Nb- and Ta-oxide nanoparticles, which are all insulators. The doping influences the resistivity, but it causes only a weak decrease in it.

Finally, we have measured the time dependence of the resistivity of the annealed films on the acetone vapour exposure, as shown in Fig. 6(d). All films show a drop in resistivity after the acetone exposure; however, the doped films show a much faster response. The best response is found for the Nb-doped film, which immediately dropped significantly after its exposure to acetone vapour.

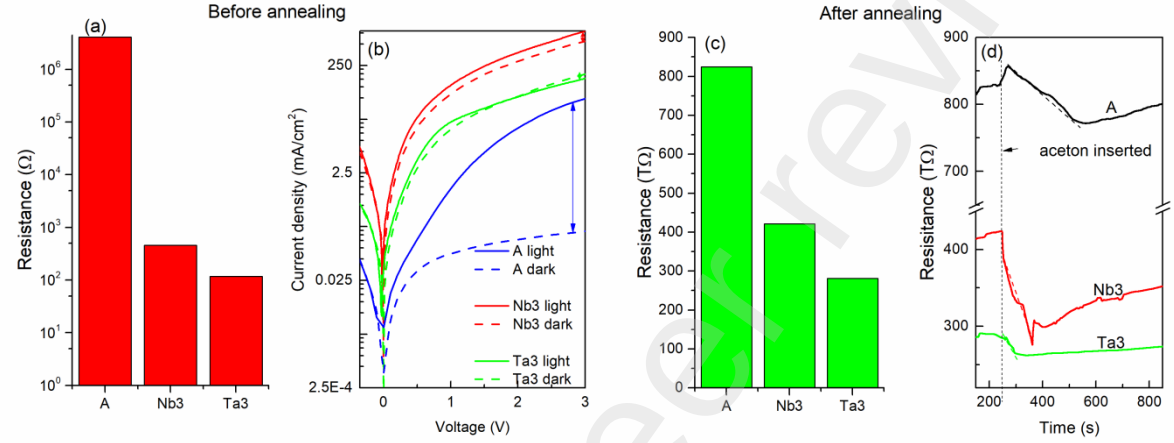

Fig. 6. Electrical properties of the films. (a) Resistance and (b) I-V characterization in the dark and under the light of the films before annealing. (c) Resistance and time dependence on acetone vapour exposure for the annealed nanoporous films.

Our preliminary measurements show that the proposed thin films containing nanoporous alumina doped with Nb could be used for conductometric gas sensors. However, further measurements are needed that would have a controlled acetone concentration and base pressure.

4. Conclusion

In this work, we have investigated two material types consisting of a 3D mesh of Ge quantum wires and nanopores in Ta- and Nb-doped alumina matrix. The influence of doping on the material structural, optical electric and acetone sensing properties are explored. We have shown that doping Ge quantum wire–based materials can tune their optical properties and decrease their resistivity. However, the mentioned doping diminishes the photo-current generation abilities of Ge quantum wires in alumina. The nanoporous material, produced by annealing the material with Ge quantum wires, has substantially different electrical and optical properties than the non-annealed one. The resistivity is several orders of magnitude higher, and the optical constants are significantly lower. That is expected due to Ge evaporation and the formation of nanopores decorated with Nb_2O_5 and Ta_2O_5 nanoparticles. These nanoporous materials, especially the Nb-doped one, show an excellent predisposition for acetone sensing. Their resistance drops firmly immediately after exposure to acetone vapour. So, we emphasize that these preliminary measurements show that the proposed porous thin films doped with Nb could be used for conductometric gas sensors. However, further measurements are needed that would have a controlled acetone concentration and base pressure.

Author Contributions: Conceptualization, M.T, and M.M.; methodology, M.T., I.P., K.S., S.B., and M.M.; software, M.M.; formal analysis, M.T., I.P, K.S., and M.M.; data curation, M.T., I.P. I.Š., M.B., S.B.; writing—original draft preparation, M.T., M.M.; writing—review and editing, all authors.; visualization, M.T. and M.M.; project administration, M.M.; funding acquisition, M.M. All authors have read and agreed to the published version of the manuscript.

Funding: This research was funded by Croatian Science Foundation (No. IP-2018-01-3633 and DOK-2018-09-5383) and the Center of Excellence for Advanced Materials and Sensing Devices (Grant KK.01.1.1.01.0001). The authors acknowledge the CERIC-ERIC Consortium for access to the experimental SAXS facilities and financial support.

Acknowledgments: The authors are thankful to J. Erceg for the assistance in the sample preparation and D. Mičetić for the GISAXS/GIWAXS measurements. The authors acknowledge the CERIC-ERIC Consortium for the access to the experimental SAXS facilities and financial support.

Conflicts of Interest: The authors declare no conflict of interest. The funders had no role in the design of the study, in the collection, analyses, or interpretation of data, in the writing of the manuscript, or in the decision to publish the results.

[1] M.C. Beard, J.M. Luther, A.J. Nozik, Multiple exciton generation in semiconductor quantum dots and electronically coupled quantum dot arrays for application to third- generation photovoltaic solar cells, 2010. https://doi.org/10.1017/CBO9781139022750.006.

[2] B. Liu, J. Hu, L. Jia, J. Liu, X. Ren, X. Zhang, X. Guo, S. (Frank) Liu, Ge quantum-dot enhanced c-Si solar cell for improved light trapping efficiency, Sol. Energy. 167 (2018) 102–107. https://doi.org/10.1016/j.solener.2018.03.074.

[3] A. Foerster, N.A. Besley, Quantum Chemical Characterization and Design of Quantum Dots for Sensing Applications, J. Phys. Chem. A. (2022). https://doi.org/10.1021/acs.jpca.2c00947.

[4] A. Lesiak, K. Drzozga, J. Cabaj, M. Bański, K. Malecha, A. Podhorodecki, Optical sensors based on II-VI quantum dots, Nanomaterials. 9 (2019) 1–24. https://doi.org/10.3390/nano9020192.

[5] S.R.C. Pinto, A.G. Rolo, M.J.M. Gomes, M. Ivanda, I. Bogdanović-Radović, J. Grenzer, A. Mücklich, D.J. Barber, S. Bernstorff, M. Buljan, Formation of void lattice after annealing of Ge quantum dot lattice in alumina matrix, Appl. Phys. Lett. 97 (2010) 1–3. https://doi.org/10.1063/1.3499426.

[6] Y.M. Niquet, G. Allan, C. Delerue, M. Lannoo, Quantum confinement in germanium nanocrystals, Appl. Phys. Lett. 77 (2000) 1182–1184. https://doi.org/10.1063/1.1289659.

[7] C. Bostedt, T. Van Buuren, T.M. Willey, N. Franco, L.J. Terminello, C. Heske, T. Möller, Strong quantum-confinement effects in the conduction band of germanium nanocrystals, Appl. Phys. Lett. 84 (2004) 4056–4058. https://doi.org/10.1063/1.1751616.

[8] X.Y. Yue, Z.J. Zhou, Y.M. Wu, Y. Li, J.C. Li, Y.H. Bai, J.L. Wang, Application Progress of Fluorescent Carbon Quantum Dots in Food Analysis, Chinese J. Anal. Chem. 48 (2020) 1288–1296. https://doi.org/10.1016/S1872-2040(20)60049-4.

[9] N. Azam, M. Najabat Ali, T. Javaid Khan, Carbon Quantum Dots for Biomedical Applications: Review and Analysis, Front. Mater. 8 (2021) 1–21. https://doi.org/10.3389/fmats.2021.700403.

[10] C. Huang, W. Xie, M. Yang, J. Dai, B. Zhang, Optical fiber Fabry-Perot humidity sensor based on porous Al2O3 film, IEEE Photonics Technol. Lett. 27 (2015) 2127–2130. https://doi.org/10.1109/LPT.2015.2454271.

[11] A. Sciuto, M.C. Mazzillo, S. Di Franco, G. Mannino, P. Badala, L. Renna, C. Caruso, G. Korotcenkov, B.K. Cho, Z.H. Zargar, T. Islam, S. Kladsomboon, T. Kerdcharoen, P. Kuang, K. Constant, A. Yamaguchi, K. Hotta, N. Teramae, S. Shaik, A.K. Tiwari, S.A. Ramakrishna, Alcohol sensor based on gold-coated nanoporous anodic alumina membrane, Anal. Chim. Acta. 81 (2019) 105–111. https://doi.org/10.5772/60798.

[12] H. Wang, X. Liu, P. Niu, S. Wang, J. Shi, L. Li, Porous Two-Dimensional Materials for Photocatalytic and Electrocatalytic Applications, Matter. 2 (2020) 1377–1413. https://doi.org/10.1016/j.matt.2020.04.002.

[13] A. Vázquez-López, J. Bartolomé, A. Cremades, D. Maestre, High-performance room-temperature conductometric gas sensors: materials and strategies, Chemosensors. 10 (2022). https://doi.org/10.3390/chemosensors10060227.

[14] K.J. Choi, H.W. Jang, One-dimensional oxide nanostructures as gas-sensing materials: Review and issues, Sensors. 10 (2010) 4083–4099. https://doi.org/10.3390/s100404083.

[15] T. Beline, J.H.D. da Silva, A.O. Matos, N.F. Azevedo Neto, A.B. de Almeida, F.H. Nociti Júnior, D.M.G. Leite, E.C. Rangel, V.A.R. Barão, Tailoring the synthesis of tantalum-based thin films for biomedical application: Characterization and biological response, Mater. Sci. Eng. C. 101 (2019) 111–119. https://doi.org/10.1016/j.msec.2019.03.072.

[16] S. Yakovin, A. Zykov, S. Dudin, N. Yefymenko, Synthesis of thin-film TA2O5 coatings by reactive magnetron sputtering, Probl. At. Sci. Technol. 106 (2016) 248–251.

[17] K.J. Kumar, N.R.C. Raju, A. Subrahmanyam, Properties of pulsed reactive DC magnetron sputtered tantalum oxide (Ta2O5) thin films for photocatalysis, Surf. Coatings Technol. 205 (2011) S261–S264. https://doi.org/10.1016/j.surfcoat.2011.03.052.

[18] N. Hossain, O. Günes, C. Zhang, C. Koughia, Y. Li, S.J. Wen, R. Wong, S. Kasap, Q. Yang, Structural and physical properties of NbO2 and Nb2O5 thin films prepared by magnetron sputtering, J. Mater. Sci. Mater. Electron. 30 (2019) 9822–9835. https://doi.org/10.1007/s10854-019-01319-8.

[19] W. Quan, X. Hu, X. Min, J. Qiu, R. Tian, P. Ji, W. Qin, H. Wang, T. Pan, S. Cheng, X. Chen, W. Zhang, X. Wang, H. Zheng, A highly sensitive and selective ppb-level acetone sensor based on a pt-doped 3D porous SnO2 hierarchical structure, Sensors (Switzerland). 20 (2020) 1–18. https://doi.org/10.3390/s20041150.

[20] P. Ma, J. Li, Y. Chen, B.A. Zhou Montano, H. Luo, D. Zhang, H. Zheng, Y. Liu, H. Lin, W. Zhu, G. Zhang, H. Mao, J. Yu, Z. Chen, Non-invasive exhaled breath diagnostic and monitoring technologies, Microw. Opt. Technol. Lett. (2021) 1–14. https://doi.org/10.1002/mop.33133.

[21] T.P.J. Blaikie, J.A. Edge, G. Hancock, D. Lunn, C. Megson, R. Peverall, G. Richmond, G.A.D. Ritchie, D. Taylor, Comparison of breath gases, including acetone, with blood glucose and blood ketones in children and adolescents with type 1 diabetes, J. Breath Res. 8 (2014). https://doi.org/10.1088/1752-7155/8/4/046010.

[22] M. Tkalčević, J. Sancho-Parramon, L. Basioli, M. Bubaš, G. Dražić, P. Nadazdy, P. Siffalovica, M. Mičetić, 3D networks of nanopores in alumina: Structural and optical properties, Microporous Mesoporous Mater. 325 (2021) 1-8. https://doi.org/10.1016/j.micromeso.2021.111306.

[23] L. Basioli, M. Tkalčević, I. Bogdanović-Radović, G. Dražić, P. Nadazdy, P. Siffalovic, K. Salamon, M. Mičetić, 3D networks of Ge quantum wires in amorphous alumina matrix, Nanomaterials. 10 (2020) 1–11. https://doi.org/10.3390/nano10071363.

[24] M. Tkalčević, D. Borščak, I. Periša, I. Bogdanović-Radović, I. Šarić Janković, M. Petravić, S. Bernstorff, M. Mičetić, Multiple Exciton Generation in 3D-Ordered Networks of Ge Quantum Wires in Alumina Matrix, Materials (Basel). 15 (2022) 13. https://doi.org/10.3390/ma15155353.

[25] L. Basioli, J. Sancho-Parramon, V. Despoja, S. Fazinić, I. Bogdanović Radović, I. Božićević Mihalić, K. Salamon, N. Nekić, M. Ivanda, G. Dražić, S. Bernstorff, G. Aquilanti, M. Mičetić, Ge quantum dots coated with metal shells (Al, Ta, and Ti) embedded in alumina thin films for solar energy conversion, ACS Appl. Nano Mater. 3 (2020) 8640–8650. https://doi.org/10.1021/acsanm.0c01333.

[26] I. Periša, M. Tkalčević, S. Isaković, L. Basioli, M. Ivanda, S. Bernstorff, M. Mičetić, Ge/Al and Ge/Si3N4/Al Core/Shell Quantum Dot Lattices in Alumina: Boosting the Spectral Response by Tensile Strain, Materials (Basel). 15 (2022). https://doi.org/10.3390/ma15186211.

[27] M. Tkalčević, M. Gotić, L. Basioli, M. Lihter, G. Dražić, S. Bernstorff, T. Vuletić, M. Mičetić, Deposition of thin alumina films containing 3D ordered network of nanopores on porous substrates, Materials (Basel). 13 (2020) 1–11. https://doi.org/10.3390/ma13132883.

[28] S.R.C. Pinto, A.G. Rolo, M.J.M. Gomes, M. Ivanda, I. Bogdanović-Radović, J. Grenzer, A. Mücklich, D.J. Barber, S. Bernstorff, M. Buljan, Formation of void lattice after annealing of Ge quantum dot lattice in alumina matrix, Appl. Phys. Lett. 97 (2010) 95–98. https://doi.org/10.1063/1.3499426.

[29] S. Shaik, A.K. Tiwari, S.A. Ramakrishna, Alcohol sensor based on gold-coated nanoporous anodic alumina membrane, Pramana - J. Phys. 93 (2019). https://doi.org/10.1007/s12043-019-1793-4.

[30] S.R.C. Pinto, A.G. Rolo, M.J.M. Gomes, M. Ivanda, I. Bogdanović-Radović, J. Grenzer, A. Mücklich, D.J. Barber, S. Bernstorff, M. Buljan, Formation of void lattice after annealing of Ge quantum dot lattice in alumina matrix, Appl. Phys. Lett. 97 (2010) 1-13. https://doi.org/10.1063/1.3499426.

[31] R. Georgiev, B. Georgieva, M. Vasileva, P. Ivanov, T. Babeva, Optical Properties of Sol-Gel Nb2O5 Films with Tunable Porosity for Sensing Applications, Adv. Condens. Matter Phys. 2015 (2015). https://doi.org/10.1155/2015/403196.

[32] S. Ezhilvalavan, T.Y. Tseng, Preparation and properties of tantalum pentoxide (Ta2O5) thin films for ultra large scale integrated circuits (ULSIs) application - a review, J. Mater. Sci. Mater. Electron. 10 (1999) 9–31. https://doi.org/10.1023/A:1008970922635.

[33] M. Buljan, N. Radić, S. Bernstorff, G. Draić, I. Bogdanović-Radović, V. Hol, Grazing-incidence small-angle X-ray scattering: Application to the study of quantum dot lattices, Acta Crystallogr. Sect. A Found. Crystallogr. 68 (2012) 124–138. https://doi.org/10.1107/S0108767311040104.

[34] V. Despoja, L. Basioli, J.S. Parramon, M. Mičetić, Optical absorption in array of Ge/Al-shell nanoparticles in an alumina matrix, Sci. Rep. 10 (2020) 1-12. https://doi.org/10.1038/s41598-019-56673-8.

[35] K. Kita, S. Suzuki, H. Nomura, T. Takahashi, T. Nishimura, A. Toriumi, Direct evidence of GeO volatilization from GeO2/Ge and impact of its suppression on GeO2/Ge metal-insulator-semiconductor characteristics, Jpn. J. Appl. Phys. 47 (2008) 2349–2353. https://doi.org/10.1143/JJAP.47.2349.

[36] S.K. Wang, K. Kita, C.H. Lee, T. Tabata, T. Nishimura, K. Nagashio, A. Toriumi, Desorption kinetics of GeO from GeO2 /Ge structure, J. Appl. Phys. 108 (2010) 1-8. https://doi.org/10.1063/1.3475990.

[37] S.R.M. Da Silva, G.K. Rolim, G. V. Soares, I.J.R. Baumvol, C. Krug, L. Miotti, F.L. Freire, M.E.H.M. Da Costa, C. Radtke, Oxygen transport and GeO 2 stability during thermal oxidation of Ge, Appl. Phys. Lett. 100 (2012) 2010–2014. https://doi.org/10.1063/1.4712619.

[38] L. Basioli, K. Salamon, M. Tkalčević, I. Mekterović, S. Bernstorff, M. Mičetić, Application of GISAXS in the investigation of three-dimensional lattices of nanostructures, Crystals. 9 (2019) 1-13. https://doi.org/10.3390/cryst9090479.

[39] I. Mekterović, G. Svalina, S. Isaković, M. Mičetić, GisaxStudio—An Open Platform for Analysis

and Simulation of GISAXS from 3D Nanoparticle Lattices, Appl. Sci. 12 (2022) 1–16. https://doi.org/10.3390/app12199773.

[40] P.K. Giri, S. Bhattacharyya, S. Kumari, K. Das, S.K. Ray, B.K. Panigrahi, K.G.M. Nair, Ultraviolet and blue photoluminescence from sputter deposited Ge nanocrystals embedded in SiO2 matrix, J. Appl. Phys. 103 (2008). https://doi.org/10.1063/1.2930877.

[41] S.D. Ponja, I.P. Parkin, C.J. Carmalt, Synthesis and material characterization of amorphous and crystalline (α-) Al2O3: Via aerosol assisted chemical vapour deposition, RSC Adv. 6 (2016) 102956–102960. https://doi.org/10.1039/c6ra24018f.

[42] S. Venkataraj, R. Drese, C. Liesch, O. Kappertz, R. Jayavel, M. Wuttig, Temperature stability of sputtered niobium-oxide films, J. Appl. Phys. 91 (2002) 4863–4871. https://doi.org/10.1063/1.1458052.

[43] R. Sagar, A. Rao, Surface modification of silicon solar cell using TiO2 and Ta2O5: fabrication and characterization, Appl. Phys. A Mater. Sci. Process. 125 (2019) 1–8. https://doi.org/10.1007/s00339-019-3161-0.

[44] M. Tkalčević, L. Basioli, K. Salamon, I. Šarić, J.S. Parramon, M. Bubaš, I. Bogdanović-Radović, S. Bernstorff, Z. Fogarassy, K. Balázsi, M. Petravić, M. Mičetić, Ge quantum dot lattices in alumina prepared by nitrogen assisted deposition: Structure and photoelectric conversion efficiency, Sol. Energy Mater. Sol. Cells. 218 (2020) 1-10. https://doi.org/10.1016/j.solmat.2020.110722.